NOTES AND CORRESPONDENCE

Three-Dimensional Wind Retrieval: Application of MUSCAT to Dual-Doppler Lidar

SUSANNE DRECHSEL,* MICHEL CHONG,+ GEORG J. MAYR,* MARTIN WEISSMANN,#
RONALD CALHOUN,@ AND ANDREAS DÖRNBRACK#

* *Institute of Meteorology and Geophysics, University of Innsbruck, Innsbruck, Austria*
+ *Laboratoire d'Aerologie, CNRS–Universite de Toulouse, Toulouse, France*
# *Deutsches Zentrum für Luft- und Raumfahrt, Institute für Physik der Atmosphäre, Oberpfaffenhofen, Germany*
@ *Department of Mechanical and Aerospace Engineering, Arizona State University, Tempe, Arizona*

(Manuscript received 23 January 2008, in final form 21 August 2008)

ABSTRACT

During the field campaign of the Terrain-induced Rotor Experiment (T-REX) in the spring of 2006, Doppler lidar measurements were taken in the complex terrain of the Californian Owens Valley for six weeks. While fast three-dimensional (3D) wind analysis from measured radial wind components is well established for dual weather radars, only the feasibility was shown for dual-Doppler lidars. A computationally inexpensive, variational analysis method developed for multiple-Doppler radar measurements over complex terrain was applied. The general flow pattern of the 19 derived 3D wind fields is slightly smoothed in time and space because of lidar scan duration and analysis algorithm. The comparison of extracted wind profiles to profiles from radiosondes and wind profiler reveals differences of wind speed and direction of less than 1.1 m s^{-1} and 3°, on average, with standard deviations not exceeding 2.7 m s^{-1} and 27°, respectively. Standard velocity–azimuth display (VAD) retrieval method provided higher vertical resolution than the dual-Doppler retrieval, but no horizontal structure of the flow field. The authors suggest a simple way to obtain a good first guess for a dual-lidar scan strategy geared toward 3D wind retrieval that minimizes scan duration and maximizes spatial coverage.

1. Introduction

The knowledge of three-dimensional (3D) wind fields and their temporal evolution is of interest in many areas of meteorology, for example, model initialization (i.e., research, operational), verification, or hazard warnings. Continuous wind field measurements can only be realized by remote sensing systems. Both sodar (Coulter and Kallistratova 2004) and radar wind profiler (e.g., Martner et al. 1993; Angevine et al. 1998) provide high-resolution 3D wind within a narrow cone.

The first instrument for volume wind measurements was Doppler radar, with backscatter from hydrometeors and occasionally insects and refractive inhomogeneities. Overviews are given in Doviak and Zrnic (1993) and Wakimoto and Srivastava (2003). First suggested by Probert-Jones (1960), Lhermitte and Atlas (1961) described the method and assumptions for the determination of horizontal wind speed and direction, and precipitation fall speed from radial velocity alone measured by a single Doppler radar. A major advance in 3D wind retrieval was made by combining two or more Doppler radars along with the continuity equation (e.g., Armijo 1969; Ray et al. 1978) as physical contraint. During the last decades, large improvements in signal processing (i.e., filtering, interpolation, and differentiating raw data) and analysis (Testud and Chong 1983; Chong et al. 1983;Chong and Testud 1983) improved the quality of the retrieved 3D wind field (Bousquet and Chong 1998), even in complex terrain (Chong and Cosma 2000). In principle all of the three wind components could be determined using three or more Doppler radars. Practically, the integration of the continuity equation is still indispensable, because (i) vertical wind speed poorly contributes to radial velocity at

Corresponding author address: Susanne Drechsel, Institute of Meteorology and Geophysics, University of Innsbruck, Innrain 52, A-6020 Innsbruck, Austria.
E-mail: Susanne.Drechsel@Student.uibk.ac.at

DOI: 10.1175/2008JTECHA1115.1

low scanning elevations, and (ii) measured vertical motion is that of precipitation particles (Ray et al. 1980). As the stability of the integration of the continuity equation strongly depends on upper and/or lower boundary conditions, various approaches of variational analysis methods have been suggested (e.g., O'Brien 1970; Chong and Testud 1983; Laroche and Zawadzki 1994, for a review of constraint choices).

During the late 1970s and 1980s, another instrument for remote volume wind sensing at a shorter wavelength was developed: (pulsed) Doppler lidar systems (Post et al. 1978; Bilbro and Vaughan 1978; Eberhard and Schotland 1980). These systems use wavelengths in the order of 100 nm to 10 μm, where backscatter is from molecules and widely dispersed aerosol particles. Aerosols are ubiquitous, but their concentration decreases away from their main source (i.e., the surface). Thin clouds may also provide sufficient backscatter. The typical range is 10 km, often less in the vertical because of the paucity of aerosols above the boundary layer. Hydrometeors strongly attenuate the lidar signal because of the extinction of the laser beam. Range resolution is typically 30–300 m for lidar and 100–1000 m for radar. With beamwidths of 0.1–1 mrad, lidar transverse resolution is 20–200 times finer than 1° (17.5 mrad) of weather radars. Contrary to radar beams, lidar has no sidelobes, thus, eliminating the ground clutter problem.

Rothermel et al. (1985) showed the feasibility of the adaption of radar analysis methods mentioned above for the retrieval of 3D wind from dual-Doppler lidar measurements. Since that time, lidar technology has improved enormously in terms of power, range, frequency stabilization, filtering methods, etc. (Weitkamp 2005). However, as operating these instruments is complicated and expensive, dual (or multiple) Doppler lidar measurements have been rare. In 2003 two mobile Doppler lidars were applied in both rural and urban areas of the United Kingdom. Lidar beams were coordinated to intersect at a very limited number of points in space in order to retrieve dispersion relevant parameters to improve dispersion models (Collier et al. 2005). During the Joint Urban 2003 field campaign, dual-Doppler lidars were operated in the flat terrain of Oklahoma, in order to study boundary layer transport and dispersion processes in the urban area of Oklahoma City (e.g., Xia et al. 2008; Newsom et al. 2008). Newsom et al. (2005) used the data to assess the accuracy of single-Doppler retrievals of microscale wind and temperature fields obtained by four-dimensional variational data assimilation. Calhoun et al. (2006) derived vertical profiles of horizontal wind (i.e., ''virtual towers'') at direction intersections of the lidar beams. Another opportunity for dual-Doppler lidar measurements was the Terrain-induced Rotor Experiment (T-REX) in the Owens Valley east of the Californian Sierra Nevada (Grubišić et al. 2008) in March and April 2006. The main scientific objective of T-REX was the comprehensive study of coupled mountain-wave–rotor–boundary layer systems. With almost continuous measurements for a 6-week period, two basically identical 2-μm coherent Doppler lidars were operated by the Arizona State University (ASU) and by the Institute of Atmospheric Physics of the German Aerospace Center (DLR), Oberpfaffenhofen, respectively.

A proven algorithm for the 3D wind retrieval from multiple Doppler radars was applied to the dual-lidar observations. We chose the Multiple Doppler Synthesis and Continuity Adjustment Technique (MUSCAT) since it provides stable solutions and can be used over complex terrain. A brief description of MUSCAT will be given in the following section. In the third section, the application to lidar data is explained. In section 4, we compare obtained wind fields retrieved from the dual-lidar measurements to other instruments, before we conclude with discussions.

2. 3D wind retrieval from weather radar: MUSCAT

MUSCAT was developed by Bousquet and Chong (1998) for 3D wind retrieval from airborne dual- or multiple-Doppler radar observations. The formulation was extended for application over both flat or complex terrain (Chong and Cosma 2000) as well as for ground-based radar systems (Chong and Bousquet 2001).

As its name implies MUSCAT retrieves the 3D wind field by combining dual-Doppler (or multiple Doppler) observations of radial velocity with the continuity equation. In the traditional approach, horizontal wind components, on the one hand, and vertical component, on the other hand, are determined in an iterative procedure (e.g., the coplane technique; Armijo 1969). However, the resulting wind field covers a smaller area compared to the full dual-Doppler coverage and may contain residual errors. The simultaneous, noniterative solution of the three wind components implemented in MUSCAT overcomes these limitations by including vertical wind speed w in each of its three parts consisting of data fit (A), continuity equation (B), and filtering (C). The MUSCAT function [Bousquet and Chong 1998, see their Eq. (4)]

$$F(u,v,w) = \int_S [A(u,v,w)+B(u,v,w)+C(u,v,w)]\,dxdy \tag{1}$$

is minimized in a least squares sense to provide Cartesian wind components u, v, and w on individual

horizontal surfaces S. Thus, a computationally inexpensive plane-to-plane solution is used instead of a fully 3D solution as in the multiple analytical Doppler (MANDOP) algorithm of Tabary and Scialom (2001). Wind on the planes is coupled in the vertical through term B, starting from the surface. The three parts (cost functions) of the MUSCAT formulation will be explained below.

Data fit term A represents the least squares fit of observed radial Doppler velocities to Cartesian wind components u, v, and w. A Cressman distance-dependent weighting function is applied for interpolation onto the Cartesian grid. Instead of prior averaging, the interpolation process is included in the data fit in order to avoid using a mean over data collected from beams of different steering angles, which would be problematical especially close to the radar. *Measured* vertical wind speed is composed of the vertical wind component and the terminal fall speed of precipitation particles. The latter is estimated from an empirical relationship with the observed and preinterpolated radar reflectivity. The second cost function, term B, is the expression for the adjustment of the mass continuity equation. Originally, the solution was based on an off-centered finite-difference scheme involving the lower, previously investigated horizontal plane for the vertical derivative term $\frac{\partial(\rho w)}{\partial z}$ (ρ is air density), which couples the horizontal planes in the vertical. For wind estimation at the first plane above the surface, vertical velocity is set to zero at the surface and horizontal winds are assumed constant between the surface and first plane. To apply the scheme to complex terrain, the computation of the continuity equation at the central grid points was replaced by balance of mass transports through all faces delimiting an individual grid box (Chong and Cosma 2000). There is zero mass flux through the bottom face of grid boxes at the (flat or complex) surface. Wind through the sidewalls of a grid box is assumed to be vertically uniform wind with a mean air density $\bar{\rho}$. Horizontal variations of both topography and wind components are assumed to be linear in each box. The cost function of the third term C acts as a low-pass filter. Its typical cutoff wavelength is 4 times the horizontal grid resolution. It provides wind components in regions where the prior analysis steps had been ill conditioned (e.g., along the radar baseline), by a regular extrapolation from surrounding well-conditioned regions. In this case of ground-based dual radars, Chong and Bousquet (2001) proposed to use an additional constraint minimizing the cross-baseline variations of the wind component normal to the radar baseline so as to reduce their geometry-induced errors. Such a constraint is applied in the present study with a weight prescribed as the fourth-power cosine of the intersection angle between the two radar beam axes at each grid point. Its formulation was not developed in Chong and Bousquet (2001), but can be found in Bousquet et al. (2008).

The 3D wind field computed in MUSCAT through a least squares analysis does not necessarily satisfy the mass conservation equation. An a posteriori upward integration of this equation was used for the final adjustment. The method proposed by Georgis et al. (2000) was applied with vertical velocity at the surface defined from a free-slip tangential velocity over orography. This method modifies the MUSCAT-derived horizontal wind components in such a way that the horizontal gradients of vertical velocity within the 3D volume as well as the vertical speed at the upper boundary are minimized. Moreover, Georgis et al. proposed to modulate the last minimization term by a weighting factor ranging from 1 to 0.5 according to the radar reflectivity factor at the top of the domain, due to strong correlation between vertical motion and radar reflectivity. In the case of dry air conditions for the present lidar observations, a constant weight of 1 is considered in the absence of a well-identified relationship between vertical velocity and backscattered lidar signal. In essence, the minimization of the vertical velocity at the top of the domain has the effect to limit its inherent amplification during the upward integration process, and it should be considered as a subsidiary constraint to the minimization of the horizontal gradients within the whole domain, as already suggested in Chong and Testud (1983).

3. MUSCAT setup for T-REX dual-Doppler lidar configuration

As MUSCAT provides a simultaneous, noniterative solution of a dual- or multiple-equation system for radar observations even in complex terrain, it was chosen for application to lidar measurements. Because of the differences between the radar and lidar systems summarized in section 1, some changes to the radar configuration of MUSCAT were necessary.

a. Topography and dataset

The north-northwest–south-southeast-oriented Owens Valley is about 150 km long and embedded between the southern part of the Sierra Nevada to the west and the White–Inyo Mountains to the east (Fig. 1). From the ridgeline with a number of peaks above 4 km MSL, the steep slopes of the Sierra Nevada drop roughly 3000 m to the valley floor, which has a width of 15–30 km. Instruments used for the present study were installed in the vicinity of the town of Independence, California, at the western side of the valley bottom, which was one of the target areas of the T-REX field campaign.

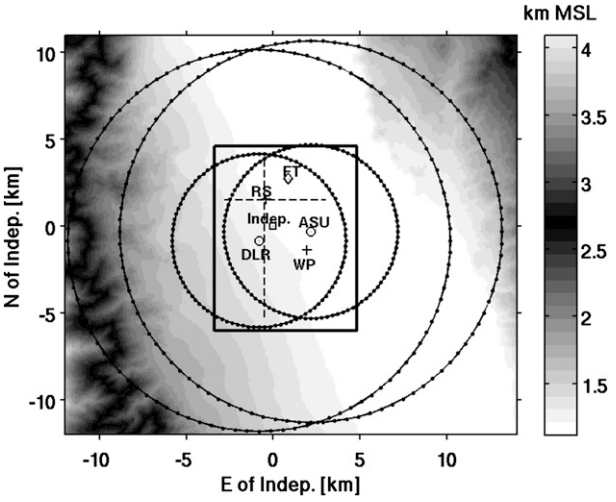

FIG. 1. Topography of Owens Valley in the Sierra Nevada with the city of Independence (Indep.) at its origin. The shaded area is the altitude MSL with elevation contour intervals drawn every 100 m. (circles) The 5- and 11-km ranges of ASU and DLR lidars, respectively. (box) The region of successful 3D wind retrieval. (dashed lines) Position of vertical cross sections. The plus signs mark the locations of WP and the launch site of RS. The flux tower (FT) is marked by a diamond.

TABLE 1. Date (day and month), begin and end (UTC time) of (DLR) volume scan (LST = UTC − 8 h in March, and LST = UTC − 7 h in April), duration T of (DLR) volume scan (UTC time), time shift dt (s) between DLR and ASU scans; number N of PPIs per volume; wind direction dd and wind speed ff (m s^{-1}) of lowest DLR scan; radiosonde RS and wind profiler WP available (x) or not (−) within a time window of ± half an hour around volume scan time. Elevation angles of volumes built from 10 PPI scans: 03°, 10°, 18°, 27°, 45°, 06°, 14°, 22°, 32°, and 60°. Elevation angles of volumes built from 12 PPI scans: 02°, 05°, 07°, 10°, 12°, 15°, 17°, 20°, 25°, 30°, 45°, and 60°.

Date	Start	End	T	dt	N	dd	ff	RS	WP
28 Mar	1359:52	1419:22	1930	8	12	SE	9	x	x
28 Mar	1759:45	1819:15	1930	12	12	SSE	16	−	x
28 Mar	1859:44	1919:14	1930	14	10	SE	19	−	x
8 Apr	2300:21	2316:12	1551	15	10	SSE	10	x	x
9 Apr	2200:05	2215:56	1551	3	10	SE	13	−	x
9 Apr	2300:06	2315:57	1551	4	10	SE	16	x	x
10 Apr	2300:02	2315:53	1551	10	10	SE	13	x	x
11 Apr	2300:02	2315:53	1551	12	10	S	14	x	x
12 Apr	0000:02	0015:53	1551	13	10	S	14	−	x
12 Apr	0030:39	0046:28	1549	35	10	S	12	−	x
12 Apr	1030:09	1045:59	1550	14	10	SE	3	−	x
12 Apr	1130:09	1145:59	1550	14	10	SE	6	−	x
12 Apr	1230:10	1246:00	1550	16	10	S	12	x	x
12 Apr	2330:10	2346:00	1550	25	10	SSE	19	x	x
13 Apr	1230:09	1246:00	1551	36	10	SW	5	x	x
13 Apr	2230:09	2246:00	1551	45	10	SE	18	x	x
14 Apr	1230:10	1246:00	1550	56	10	SE	11	x	x
16 Apr	1350:12	1406:02	1550	7	10	SSE	6	x	x
17 Apr	2250:12	2306:02	1550	5	10	N	9	x	x

The 2-μm Doppler lidars were installed about 0.5–1 km south of Independence, with the DLR lidar in the west at the foothills of the Sierra Nevada at an altitude of 1241 m MSL, and the ASU lidar to the east at the quasi-flat valley bottom at an altitude of 1179 m MSL. The orientation of the 3-km baseline was almost perpendicular to the valley axis, in an angle of roughly 80° from north.

Dual-lidar data are available for the period between 14 March and 25 April 2006. The lidars scanned either at fixed elevation and varying azimuth angles [plan position indicator (PPI), approximately 25%], or vice versa [range–height indicator (RHI), approximately 75%]. The range gates of the DLR lidar had a length of 105 m with the center of the first gate at 396 m, the range gates of the ASU lidar had a length of 85 m with the first gate at 441 m. With 100 range gates per beam, the absolute maximum range was 11 or 9 km, respectively, for the DLR and the ASU lidar (for more details see WindTracer online at www.Lockheedmartin.com/ssc/coherent/products/windtracer/Specifications.html, the specification data sheet of Lockheed Martin Coherent Technologies, the manufacturer of both lidars). Using azimuth angle intervals of 3°–5° and an averaging time of 1 s for a beam, the scan duration of a complete PPI was approximately 100–120 s. The datasets for MUSCAT were chosen according to the criteria of (i) large spatial coverage, (ii) synchronously scanning ASU and DLR lidars, (iii) quasi-stationary wind conditions during scan duration, and (iv) availability of (vertically extended) comparison data (i.e., radio soundings and wind profiler) within half an hour around the lidar scan times. Only 19 datasets (called ''volumes'' hereafter) fulfilled these criteria. In 12 cases both radio sounding and wind profiler data were available for comparison; only wind profiler data were available for the remaining seven cases. The volumes were built from 10 and 12 PPI scans, respectively (Table 1). The volume scan took between 16 and 20 min to complete, about 2–3 times as long as typical weather radar scans. The measurement of the same azimuth and elevation angle (ASU and DLR) could differ by up to 3 min. Because of the altitude difference of the lidar sites there were practically no simultaneously sampled, collocated range gates. Nevertheless, because of the quasi-stationarity of the wind fields during each volume scan (cf. section 5), the time shift and scan duration are within an acceptable range.

b. MUSCAT setup

Apart from omitting terminal fall speed in MUSCAT, the required adjustments are due to the differences in

(i) resolution and (ii) range of the measurements, as well as in (iii) applied scan strategy.

In general, the higher transverse and longitudinal resolution of lidar observations allows a refinement of the horizontal grid onto which the data are interpolated within the data fit procedure, yielding a higher resolution of the 3D wind field compared to the results from radar observations. Higher computational cost for the refined grid is neutralized by the smaller total horizontal grid size caused by the shorter range of lidar measurements. In the vertical, the extent and mesh width of the grid depend on the applied scanning strategy. Sampling in the middle and upper troposphere requires higher scanning elevations of lidar compared to radar, again because of the lower range. For example the necessary elevation angle to obtain a return at 5 km above ground is 15.7° for typical horizontal radar distance of 50 km, but 45° for a typical horizontal lidar distance of 5 km. The elevation steps of the lidar scans determine the vertical grid spacing. A popular scanning strategy is to increase the steps with increasing height in order to save time. This strategy is justified by the assumption that wind at higher elevation is more homogeneous than near the surface. For setting the vertical grid spacing, the mean vertical distances between the observations should be considered.

Finally, horizontal and vertical radii of influence for the Cressman weighting function have to be adapted, with radii larger than the resolution of observations and equal to or larger than grid spacing.

With range gates of approximately 100 m, the longitudinal beam resolution of the T-REX lidars was about one-fifth of that of the radars. The usual MUSCAT grid resolution of 1.5 km in the horizontal and 0.5 km in the vertical dimension (e.g., Chong and Bousquet 2001) was set to 0.2 km in all three dimensions. The vertical grid spacing was set according to the mean vertical distance between observations within a 5-km radius around the lidar at elevation angles below 45°. As maximum lidar range is about one-sixth of the maximum radar range, the usual domain of MUSCAT wind retrieval was reduced from 75 km × 75 km × 14.5 km (length, width, and height, respectively) to a box of 10 km × 11 km × 4 km. Setting horizontal and vertical radii of influence, a compromise was sought between retaining small-scale features of the original radial velocity fields and maximizing the coverage of the retrieved 3D wind field. While in a weather radar application radar volumes can be built from PPI scans at 20 different elevations between −0.3° and 40° (e.g., Joss et al. 1999), the T-REX lidars measured only at 10–12 elevation angles between 2° and 60° (Table 1). Horizontal and vertical radii of 250, 500, 750, and 1000 m were tested. The comparison to radio sounding and wind profiler showed that radii of 1000 m in the horizontal and 500 m in the vertical were the best compromises. With those radii, the box of successful wind retrieval has a size of roughly 8 km (east–west) × 10.5 km (north–south) × 3.5 km (vertical).

4. Comparison of MUSCAT wind fields to other measurements

For verification of MUSCAT wind fields, wind data of Vaisala RS80 GPS radiosondes (RS) launched at Independence airport by the University of Leeds, and of a wind profiler (WP) operated by the National Center for Atmospheric Research (NCAR) about 0.5 km south of the ASU lidar site, were analyzed (Fig. 1). Both vertical and horizontal resolution differs from MUSCAT: between 3 and 16 m and 3 s for RS; 100-m and 30-min averages for WP, resulting in differences between wind profiles of RS and WP. To eliminate the difference in the vertical resolution, RS and WP are averaged to the heights of the MUSCAT levels using the radii of influence applied in MUSCAT.

To get an estimate of possible differences caused by the differing temporal resolutions, the variability of wind during the lidar scan periods was computed from 10-Hz wind data of the 3D ultrasonic R. M. Young 81000 anemometer installed at the height of 11.4 m above ground on the ASU flux tower at the ASU lidar site. The temporal variability is discussed in section 5.

DLR lidar data of the 19 volumes ingested to MUSCAT were also used to retrieve 19 vertical profiles of horizontal wind based on the velocity–azimuth display (VAD) technique (Browning and Wexler 1968). The profiles are compared to MUSCAT wind as well as to RS and WP by averaging VAD values to the heights of RS or WP data.

Additionally to RS and WP data, vertical wind speed w was also determined from vertically directed beams (90° ± 1° elevation angle) of the DLR RHIs succeeding the volume scans. These measurements were at maximum 3 min after the last PPI scan. It should be noted that w is more difficult to evaluate than horizontal wind because of its order of magnitude, which is about one-fifth to one-tenth of that of horizontal wind, as well as its sensitivity to temporal and spatial averaging.

In all of the 19 available comparison periods there was no precipitation in the vicinity of the lidars. In the valley, southerly winds prevailed during 18 cases, with westerly to southwesterly winds at the crest level. The exception was 17 April with northerly winds in the valley and northwesterly winds aloft. In 12 of 19 cases (including that with northerly wind), WP profiles clearly

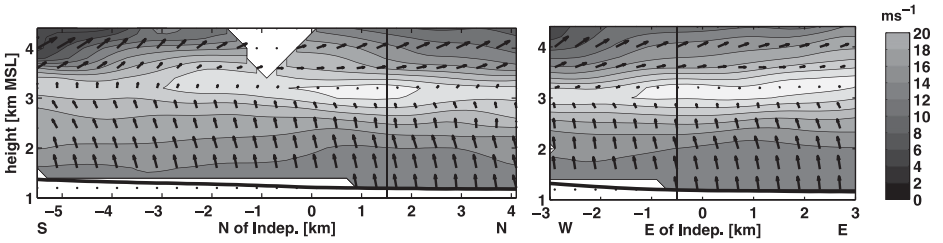

FIG. 2. MUSCAT-retrieved wind fields at 2300 UTC (1600 LST) 11 Apr 2006. (left) Vertical south–north cross section 0.5 km west of Independence and (right) vertical west–east cross section 1.5 km north of Independence. Vertical black lines mark intersection of cross sections. Wind vectors of horizontal wind are shown at every other grid point. The reference wind vector shows a 20 m s^{-1} southerly wind. Wind speed is shaded.

indicate a channeling structure [i.e., high wind speeds (exceeding at least 9 m s^{-1})] in a layer of roughly 1000 m of thickness at the bottom, with weaker winds aloft. This flow pattern is captured by MUSCAT, as shown by two vertical cross sections (south–north and west–east) of MUSCAT fields for 2300 UTC (1600 LST) 11 April (Fig. 2). At horizontal planes, the wind field is not uniform, but mostly shows stronger winds near the Sierra Nevada to the western edge of the MUSCAT domain, especially at higher levels. An example of this horizontal structure is shown in Fig. 3, where two horizontal cross sections at 3 and 3.4 km MSL are depicted for the same case as in Fig. 2.

The comparison of MUSCAT fields to the 12 profiles of RS and the 19 profiles of WP yielded the following results.

a. Horizontal wind

Relatively small biases in both wind speed and direction (Table 2) were found for horizontal wind derived from MUSCAT and RS, and MUSCAT and WP profiles, respectively (one example profile of each is depicted in Fig. 4). On average, MUSCAT wind speed is 1.0 m s^{-1} lower than in WP (mean wind speed 10.9 m s^{-1}, 19 cases), and 0.1 m s^{-1} higher than RS (mean wind speed 8.0 m s^{-1}, 12 cases). The wind direction of

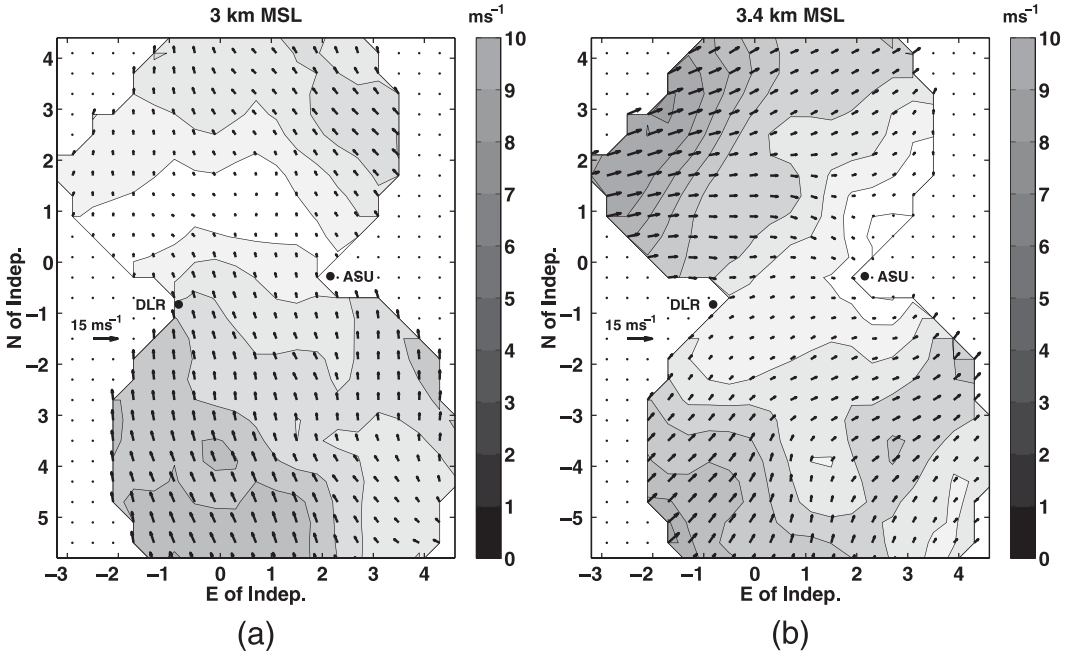

FIG. 3. MUSCAT-retrieved wind fields at 2300 UTC (1600 LST) 11 Apr 2006. Horizontal cross section at (left) 3 km MSL and (right) 3.4 km MSL. Wind vectors of horizontal wind are shown at every other grid point. The reference wind vector shows a 15 m s^{-1} westerly wind. Wind speed is shaded.

TABLE 2. Standard deviation (std dev), bias (i.e., average over differences), mean (i.e., average over absolute values of differences), and 95% percentiles (p95) of differences in wind speed (ff), wind components (u and v), and wind direction (dd), between MUSCAT (M) dual lidar and RS or WP, respectively, of all 12 (RS) or 19 (WP) profiles.

	ff (m s^{-1})	u (m s^{-1})	v (m s^{-1})	dd (°)
Std dev (RS-M)	2.7	2.5	2.5	27
Bias (RS-M)	−0.1	0.4	−0.1	2
Mean (RS-M)	2.0	1.7	1.7	15
p95 (RS-M)	5.4	5.7	5.7	37
Std dev (WP-M)	2.3	2.2	2.2	19
Bias (WP-M)	1.0	−0.1	1.2	0
Mean (WP-M)	2.0	1.6	2.0	12
p95 (WP-M)	4.9	3.9	4.6	20

MUSCAT deviates less than 1° from that of WP, and roughly 2° from that of RS.

Of course, individual differences between MUSCAT and RS/WP profiles are larger. Mainly three factors are responsible. First, MUSCAT and WP perform both a spatial and temporal averaging and smoothing, albeit over different altitudes and different times. Their beginning and ending times as well as duration of the averaging vary in general. The RS is not averaged in time, but in space using the same vertical radius of influence as in MUSCAT to enable comparability to MUSCAT. A rough estimate for the effects of temporal smoothing can be gleaned from the variability in 10-Hz wind data of the ASU flux tower. Standard deviations of wind speed and direction were approximately 1.4 m s^{-1} and 9°, respectively, over a typical scan period of 16 min. It explains approximately one-third to one-half of the magnitude of the standard deviations found in the differences between MUSCAT and WP (~2.3 m s^{-1}, 19°), or RS (~2.7 m s^{-1}, 27°), respectively. While smoothing in space mainly affects regions of vertical wind shear (Fig. 4a, 3000–3400 m MSL), smoothing in time is mainly found when such regions were vertically shifted, as well as for periods of more variable winds. Differences between MUSCAT and WP data (e.g., Fig. 4b, 1200–2200 and 3000–4400 m MSL) are difficult to trace to smoothing either in time or space.

The second factor responsible for larger differences is the poorer quality of MUSCAT data at upper and lower boundaries of the volumes, due to the paucity of the data there. This causes outliers defined by the 95% percentile of 5.4 m s^{-1} in speed and 37° in direction. The third factor is a possible nonconcurrency of the measurements from the different platforms.

Horizontal variations in the flow field depicted by MUSCAT (Fig. 3) are mostly confirmed by RS and WP as seen in Fig. 4 above the layer of wind shear: The altitude range where wind speeds increase strongly is about 400 m lower in the northern part of the MUSCAT domain (3–4 km MSL), where the RS profile was taken, than in the southern part (3.4 −4.4 km MSL), where WP is located (Fig. 1). MUSCAT reproduces that altitude difference, which can also be identified in the wind direction change.

VAD-retrieved winds are averages over the circular area enclosed by the lidar scan. Contrary to MUSCAT, they do not contain information about the horizontal flow structure. We therefore compared only the area-median value of MUSCAT with the VAD values in Fig. 5. Additionally, shown with horizontal whiskers are the 10% and 90% percentiles of MUSCAT wind components over the whole MUSCAT domain at the particular level. The VAD scans give some indication of the horizontal flow variability since various combinations of range gates and elevation angles are located at nearly the same altitude, but encompass differing areas over which the flow is averaged. This causes the scatter of the VAD points in Fig. 5. Shape and magnitude of the horizontal wind component profiles in Fig. 5 and the other profiles (not shown) are similar between the MUSCAT and VAD.

b. Vertical wind

Because of its order of magnitude and its sensitivity to temporal and spatial averaging, the vertical wind component w was not evaluated in detail. For RS, w could only be estimated from the difference of mean ascent rate averaged over the (successful) vertical MUSCAT retrieval domain, and individual ascent rates between each measurement. The amount of data is almost equal for MUSCAT, WP, and the RHI vertically directed beams (called RHI90 hereafter) with roughly 200 values. The RS has about 5300 values.

On average, downward motion dominates in the 12 profiles of MUSCAT, WP, and RHI90. The overall mean is at −0.52 m s^{-1} twice as large for the WP as for MUSCAT (−0.24 m s^{-1}). RHI90 lies in between (−0.32 m s^{-1}). For RS, average vertical wind speed is 0 due to its calculation method. The distribution of w is skewed to downdraft values for all MUSCAT, RHI90, RS, and WP (skewness of −0.08, −0.06, −0.02, and −0.25 m s^{-1}, respectively). Though the 12 investigated profiles are from channeling cases, the dominating downward motion in the region of the profiles may be ascribed to the leeward downdraft of westerly/southwesterly flow at the crest level. Compared to MUSCAT, RS, and RHI90, when regarding skewness, the relatively (strong) shift of WP vertical winds to negative values may be explained by a downward bias of WP, already described by

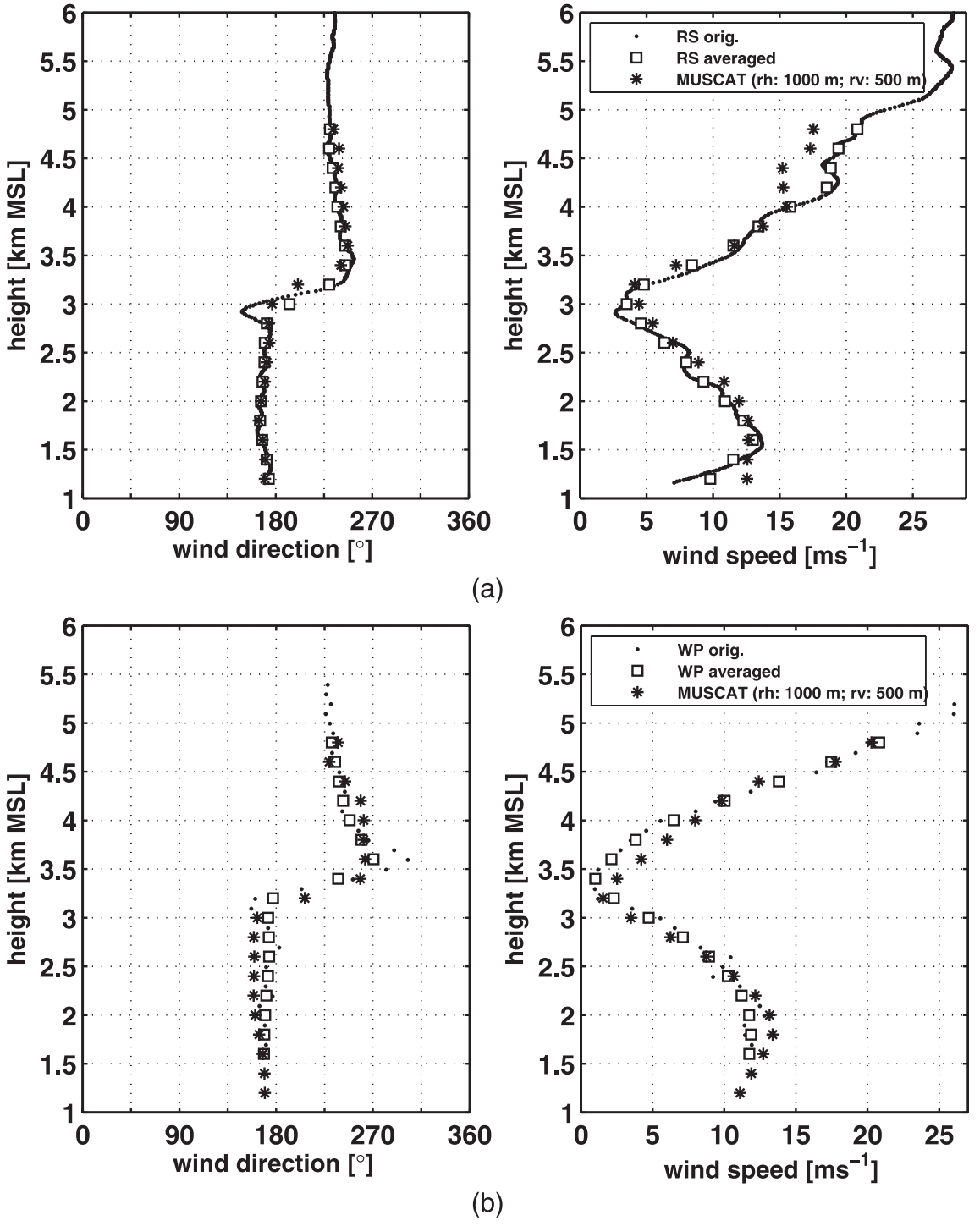

FIG. 4. Profiles of wind direction (deg) and speed (m s^{-1}) of (a) MUSCAT and radiosonde RS, and (b) MUSCAT and wind profiler WP at 2300 UTC (1600 LST) 11 Apr 2006. (stars) MUSCAT dual lidar, (small dots) original RS/WP, and (squares) RS/WP averaged to height of MUSCAT grid points using same radii of influence as applied in the MUSCAT algorithm.

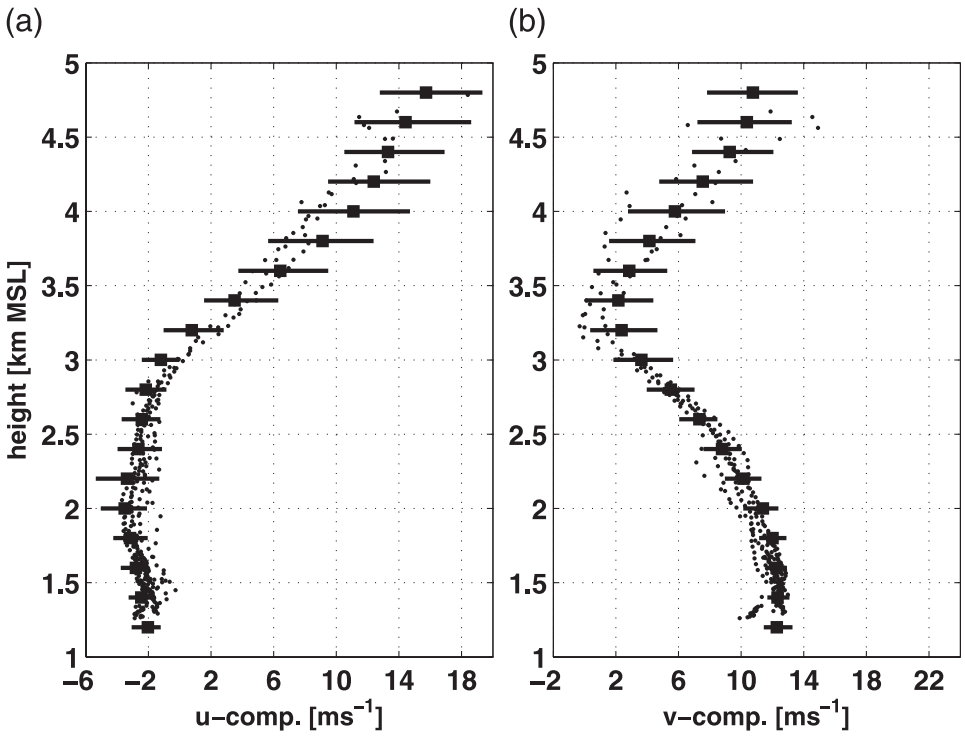

FIG. 5. Profiles of VAD- and MUSCAT-retrieved wind componentes (a) u and (b) v (m s^{-1}) at 2300 UTC (1600 LST) 11 Apr 2006. (small dots) VAD-retrieved wind from all PPIs of volume ingested to MUSCAT, (squares) median of MUSCAT wind components over the whole MUSCAT domain at the particular level, and (bars) range between (left) 10% and (right) 90% percentiles.

Angevine (1997) and Lothon et al. (2002). They found erroneous downward velocities in the range of 0.1–0.3 m s^{-1} for the convective boundary layer during the daytime. Seven of the 12 profiles are soundings in the midafternoon local time.

5. Discussion and conclusions

The work presents the application of a fast analysis technique for 3D wind retrieval, which was originally developed for radar measurements, to dual-Doppler lidar observations. The retrieved wind fields represent the general flow pattern, including changes in wind speed and direction with height. On average, wind speed and direction of MUSCAT profiles deviate 1.0 m s^{-1} and less than $-1°$ from wind of the wind profiler and only -0.1 m s^{-1} and 2° from wind of the radiosonde. Differences between individual profile grid points of MUSCAT and WP or RS, respectively, stem from limited precision of the sensors, and different spatial and temporal resolutions of the measuring systems.

For two collocated wind profilers Weber et al. (1990) found standard deviations of 2.2 and 2.3 m s^{-1} for the wind components u and v. Almost similar standard deviations between MUSCAT and WP components suggest that they should be partly associated with the precision of WP. For RS, the manufacturer claims wind errors not more than 0.3 m s^{-1} (Jaatinen and Elms 2000), which explains at most one-tenth of the differences between MUSCAT and RS. Differing spatial and temporal resolutions seem to be more critical.

The RS is an ''in situ'' measuring a ''high-resolution'' (3–16 m) instrument that samples a pseudovertical line profile. It is ''pseudo'' since the sonde is also shifted in the horizontal by the wind. The WP observes along (nearly) vertical lines with a resolution of 100 m, but needs long averaging times of 15–30 min to ensure data quality. Lidar data ingested to MUSCAT are volume measurements with a resolution of ~100 m along the lidar beam. Vertical distance between observations does not only increase with increasing distance to the lidar, but also with increasing elevation because of the scan strategy (the maximal vertical distance between lidar beams exceeds 3.6 km for a maximum range of 10 km). Though each individual lidar observation is a quasi-instantaneous value (500-Hz sample rate with 500-sample averaging), the scan duration of roughly 16 min makes the wind field retrieved by MUSCAT ''smoothed'' in time.

TABLE 3. As in Table 2, but for differences between VAD-retrieved profiles and RS or WP, respectively, of all 12 (RS) or 19 (WP) profiles.

	ff (ms^{-1})	u ($m\ s^{-1}$)	v ($m\ s^{-1}$)	dd (°)
Std dev (RS-VAD)	2.9	2.3	2.4	25
Bias (RS-VAD)	0.2	1.0	0.2	−2
Mean (RS-VAD)	2.0	1.8	1.6	15
p95 (RS-VAD)	6.3	5.1	4.8	45
Std dev (WP-VAD)	3.1	2.6	2.9	25
Bias (WP-VAD)	1.4	−0.5	1.4	1
Mean (WP-VAD)	2.7	1.9	2.6	15
p95 (WP-VAD)	6.0	5.0	5.7	58

Stationarity hypothesis is implicitly considered, so the temporal variations may be viewed as spatial variations so that they could be filtered out by the MUSCAT processing. It should be noted that MUSCAT was successfully applied to airborne radar observations of MCSs within a time delay of 80–110 min (Bousquet and Chong 2000). In a long-term comparsion of radiosondes and wind profiler, Weber and Wuertz (1990) found standard deviations of 4.6 and 4.7 m s^{-1} for the (unfiltered) wind components u and v, respectively, with wind speed from RS 0.5 to 1.0 m s^{-1} higher than from WP. The investigation of the 12 profiles of RS, and those of WP coincident in time (± half an hour) used for MUSCAT evaluation, reveals slightly lower standard deviations (3.2 and 4.2 m s^{-1}), but wind speeds higher in WP measurements. The differences between MUSCAT and the RS may (partly) result from the differing temporal resolution: They have one-third to one-half of the magnitude as standard deviations of wind speed and direction of the 10-Hz ultrasonic anemometer measurements of wind variability in 16 min. As horizontal wind fields were rather homogeneous for the investigated cases, horizontal smoothing of MUSCAT winds is negligible for differences between RS and MUSCAT, even though the horizontal distance between RS and MUSCAT grid point to be compared partly exceeded 1 km because of the RS drift. However, small-scale vertical variations like thin layers of wind shear are smoothed out by MUSCAT, leading to larger differences. These differences are also found in comparison to WP, albeit not as strongly because of a WP resolution of only 100 m. The WP values are temporally averaged over 30 min, whereas dual-lidar measurements are instantaneous but take ~20 min to scan the necessary volume. This makes a comparison of WP and MUSCAT profiles difficult. Finally, low-pass filtering with a cutoff wavelength of 4 times the horizontal grid spacing in the MUSCAT algorithm is another reason for smoothing. Wind structures of scales lower than the grid spacing are filtered out. So subgrid turbulent structures are not retrieved and MUSCAT results are representative of higher-scale or mean winds, and they strongly depend on the size of the grid (as well as the radii of influence).

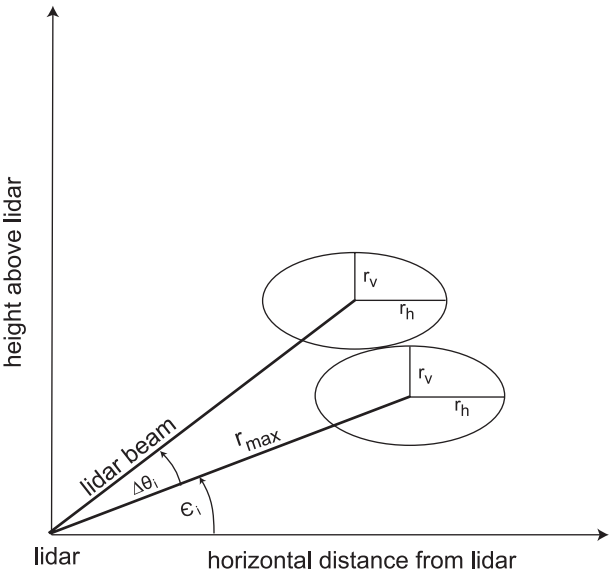

FIG. 6. Ellipsoides with half axes determined by the radii of influence r_v and r_h at two (vertical) successive beams touch each other at the distance r_{max}. The lower beam is at elevation angle ε_i, with elevation step $\Delta\theta_i$ to the upper beam.

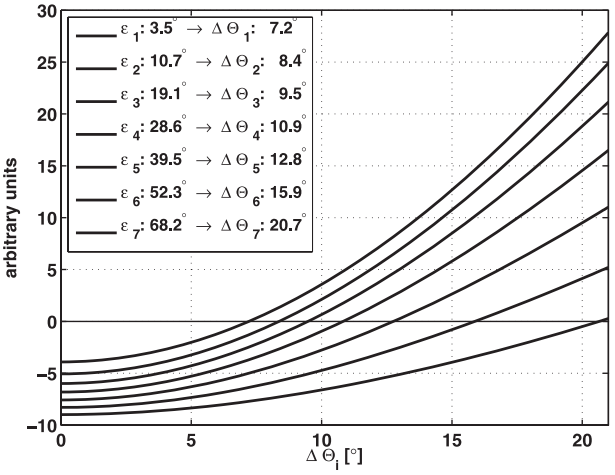

FIG. 7. Graphical depiction of the lhs of Eq. (2) for the determination of the largest possible step in elevation angle $\Delta\theta_i$ of a lidar scan to still obtain sufficient coverage for the MUSCAT retrieval of 3D wind. Solutions for several starting elevations ε_i are shown. A typical decrease of maximum range r_{max} of Eq. (2) with height is assumed: from 8 km at bottom (black curve) to roughly 5 km at PPI of 67.9° (light gray curve). Here $\Delta\theta_i$ is found at the intersection of the appropriate curve with zero on the ordinate. Starting elevation angles ε_i (deg) and appropriate $\Delta\theta_i$ (deg) are summarized in the legend.

Comparing profiles of VAD and RS/WP in the same way as MUSCAT and RS/WP showed that the differences in wind speed and direction are in general slightly higher for VAD than for MUSCAT (Table 3). Though standard VAD retrieval method provides higher vertical resolution, the striking advantage of MUSCAT is to provide both vertical and horizontal structures of the wind field with similar accuracy as VAD.

From a statistical point of view, the sample size of comparisons between MUSCAT lidar and WP and RS is small. The scanning strategy during the T-REX field campaign was geared not primarily toward optimal 3D wind retrieval, but toward the observation of mountain waves coupled with downslope windstorms and (channeled) flow in the valley. This was satisfied using mainly RHI scans at azimuth angles perpendicular and parallel, respectively, to the valley axis. Only 25% of the lidar data sampled during observation period were PPI scans. Of this still very large sample only a fraction could be used for MUSCAT. There were volumes consisting only of three or four PPIs, PPIs consisting of only 90° or 120° segments, change of the wind regime/unstationary wind field during volume scan duration (i.e., scan duration was too long), or a very short maximum range due to the lack of backscatter. Finally, (quality checked) wind profiler and radiosonde data for comparison were available for only 19 dual-Doppler volume measurements.

Based on the experience from T-REX we developed a simple way to obtain a good first guess for a scan strategy geared toward 3D wind retrieval. The two design goals are maximum spatial coverage and temporal resolution. This scan strategy is obtained by determining the elevation steps $\Delta\theta_i$ between two successive PPIs depending on (previously determined) actual maximum range $r_{\max}$ at this elevation, as well as horizontal and vertical radii of influence r_v and r_h. The latter are set according to the spatial scale of the phenomenon of interest with lower bounds stemming from the lengths of the lidar range gates, while $r_{\max}$ comes from actual measurements (e.g., at the beginning of a campaign or from experience in similar settings). To ensure complete spatial coverage, the ellipsoides with half axes determined by the radii of influence r_v and r_h at two (vertical) successive beams should just touch each other at the distance $r_{\max}$ (Fig. 6). This requirement can be written by the implicit equation for the difference between the elevation angles of successive PPIs, $\Delta\theta_i$

$$r_v^2\left[\sin\left(\frac{\Delta\theta_i}{2}\right)\sin\left(\frac{\Delta\theta_i}{2}+\varepsilon_i\right)\right]^2 + r_h^2\left[\sin\left(\frac{\Delta\theta_i}{2}\right)\cos\left(\frac{\Delta\theta_i}{2}+\varepsilon_i\right)\right]^2 - \left(\frac{r_v r_h}{r_{\max}}\right)^2 = 0, \quad (2)$$

where ε_i is the elevation angle of PPI_i. It is determined by $\sin(\varepsilon_1) = r_v/r_{\max}$ for the lowest PPI above ground. The implicit equation can be solved numerically or graphically.

An example of optimal scan strategy for a maximum lidar range decreasing with height (8 km near ground and 5 km in the vertical, which are typical ranges of T-REX measurements) is shown in Fig. 7. Radii of influence are the same as applied for T-REX lidar dataset (r_h = 1 km and r_v = 0.5 km). Only seven PPI scans (at 3.5°, 10.7°, 19.1°, 28.6°, 39.4°, 52.1°, and 67.9°) cover the total half space except for a small cone directly above the lidar at a scan elevation of 89°, as dual-/multiple-lidar measurements usually do not intersect for such elevations. Compared to T-REX volume scans consisting of 10 (12) PPIs, this strategy is roughly 30% (40%) faster, which allows us to investigate more variable wind situations. In ongoing work, we replace the real atmosphere with the virtual one of numerical models simulating actual flow situations to explore possible improvements to both the MUSCAT lidar algorithm and scan strategy.

Acknowledgments. This study is supported by the Austrian Science Fund FWF under Grant P18940. Data used in this study were gathered as part of the Terrain-induced Rotor experiment (T-REX). The primary sponsor of T-REX was the U.S. National Science Foundation. The acquisition of this radiosonde data was carried out by workers at the Institute for Atmospheric Science, University of Leeds, United Kingdom, and was funded by the Natural Environment Research Council (NERC), United Kingdom. Thanks to Ralph Burton and his team of the University of Leeds for helping with all our concerns of the radiosonde. We are grateful to William Brown and his team from NCAR for providing the wind profiler data, with special thanks for spending a lot of time on extra quality control. We are indebted to Alexander Gohm from the University of Innsbruck for providing the VAD analysis code.

REFERENCES

Angevine, W. M., 1997: Errors in mean vertical velocities measured by boundary layer wind profilers. *J. Atmos. Oceanic Technol.,* **14,** 565–569.

——, P. S. Bakwin, and K. J. Davis, 1998: Wind profiler and RASS measurements compared with measurements from a 450-m-tall tower. *J. Atmos. Oceanic Technol.,* **15,** 818–825.

Armijo, L., 1969: A theory for the determination of wind and precipitation velocities with Doppler radars. *J. Atmos. Sci.,* **26,** 570–573.

Bilbro, J. W., and W. W. Vaughan, 1978: Wind field measurement in the nonprecipitous regions surrounding severe storms by an

airborne pulsed Doppler lidar system. *Bull. Amer. Meteor. Soc.,* **59,** 1095–1100.

Bousquet, O., and M. Chong, 1998: A Multiple-Doppler Synthesis and Continuity Adjustment Technique (MUSCAT) to recover wind components from Doppler radar measurements. *J. Atmos. Oceanic Technol.,* **15,** 343–359.

——, and ——, 2000: The oceanic mesoscale convective system and associated mesovortex observed 12 December 1992 during TOGA-COARE. *Quart. J. Roy. Meteor. Soc.,* **126,** 189–211.

——, P. Tabary, and J. Parent-du Châtelet, 2008: Operational multiple-Doppler wind retrieval inferred from long-range radial velocity measurements. *J. Appl. Meteor. Climatol.,* **47,** 2929–2945.

Browning, K. A., and R. Wexler, 1968: The determination of kinematic properties of a wind field using Doppler radar. *J. Appl. Meteor.,* **7,** 105–113.

Calhoun, R., R. Heap, M. Princevac, R. Newsom, H. Fernando, and D. Ligon, 2006: Virtual towers using coherent Doppler lidar during the Joint Urban 2003 Dispersion Experiment. *J. Appl. Meteor.,* **45,** 1116–1126.

Chong, M., and J. Testud, 1983: Three-dimensional wind field analysis from dual-Doppler radar data. Part III: The boundary condition: An optimum determination based on a variational concept. *J. Climate Appl. Meteor.,* **22,** 1227–1241.

——, and S. Cosma, 2000: A formulation of the continuity equation of MUSCAT for either flat or complex terrain. *J. Atmos. Oceanic Technol.,* **17,** 1556–1565.

——, and O. Bousquet, 2001: On the application of MUSCAT to a ground-based dual-Doppler radar system. *Meteor. Atmos. Phys.,* **78,** 133–139.

——, J. Testud, and F. Roux, 1983: Three-dimensional wind field analysis from dual-Doppler radar data. Part II: Minimizing the error due to temporal variation. *J. Climate Appl. Meteor.,* **22,** 1216–1226.

Collier, C. G., and Coauthors, 2005: Dual-Doppler lidar measurements for improving dispersion models. *Bull. Amer. Meteor. Soc.,* **86,** 825–838.

Coulter, R. L., and M. Kallistratova, 2004: Two decades of progress in sodar techniques: A review of 11 ISARS proceedings. *Meteor. Atmos. Phys.,* **85,** 3–19.

Doviak, R. J., and D. S. Zrnic, 1993: *Doppler Radar and Weather Observations*. 2nd ed. Academic Press, 562 pp.

Eberhard, W. L., and R. M. Schotland, 1980: Dual-frequency Doppler-lidar method of wind measurement. *Appl. Opt.,* **19,** 2967–2976.

Georgis, J. F., F. Roux, and P. H. Hildebrand, 2000: Observation of precipitating systems over complex orography with meteorological Doppler radars: A feasibility study. *Meteor. Atmos. Phys.,* **72,** 185–202.

Grubišić, V., and Coauthors, 2008: The Terrain-induced Rotor Experiment: An overview of the field campaign and some highlights of special observations. *Bull. Amer. Meteor. Soc.,* **89,** 1513–1533.

Jaatinen, J., and J. B. Elms, 2000: On the windfinding accuracy of Loran-C, GPS and radar. *Vaisala News Mag.,* **152,** 30–33. [Available online at http://www.vaisala.com/newsandmedia/vaisalanews/archive/.]

Joss, J., and Coauthors, 1999: Operational use of radar for precipitation measurements in Switzerland. Meteo Svizzera, 121 pp.

Laroche, S., and I. Zawadzki, 1994: A variational analysis method for retrieval of three-dimensional wind field from single-Doppler radar data. *J. Atmos. Sci.,* **51,** 2664–2682.

Lhermitte, R. M., and D. Atlas, 1961: Precipitation motion by pulse Doppler radar. Preprints, *Ninth Weather Radar Conf.*, Kansas City, MO, Amer. Meteor. Soc., 218–223.

Lothon, M., B. Campistron, S. Jacoby-Koaly, B. Bénech, F. Lohou, and F. Girard-Ardhuin, 2002: Comparison of radar reflectivity and vertical velocity observed with a scannable C-band radar and two UHF profilers in the lower troposphere. *J. Atmos. Oceanic Technol.,* **19,** 899–910.

Martner, B., and Coauthors, 1993: An evaluation of wind profiler, RASS, and microwave radiometer performance. *Bull. Amer. Meteor. Soc.,* **74,** 599–613.

Newsom, R. K., D. Ligon, R. Calhoun, R. Heap, E. Cregan, and M. Princevac, 2005: Retrieval of microscale wind and temperature fields from single- and dual-Doppler lidar data. *J. Appl. Meteor.,* **44,** 1324–1345.

——, R. Calhoun, D. Ligon, and J. Allwine, 2008: Linearly organized turbulence structures observed over a suburban area by dual-Doppler lidar. *Bound.-Layer Meteor.,* **127,** 111–130.

O'Brien, J., 1970: Alternative solutions to the classical vertical velocity problem. *J. Appl. Meteor.,* **9,** 197–203.

Post, M. J., R. L. Schwiesow, R. E. Cupp, D. A. Haugen, and J. T. Newman, 1978: A comparison of anemometer- and lidar-sensed wind velocity data. *J. Appl. Meteor.,* **17,** 1179–1181.

Probert-Jones, J. R., 1960: Meteorological use of pulse Doppler radar. *Nature,* **186,** 271–273.

Ray, P. S., K. K. Wagner, K. W. Johnson, J. J. Stephens, W. C. Bumgarner, and E. A. Mueller, 1978: Triple-Doppler observations of a convective storm. *J. Appl. Meteor.,* **17,** 1201–1212.

——, C. L. Ziegler, W. Bumgarner, and R. J. Serafin, 1980: Single- and multiple-Doppler radar observations of tornadic storms. *Mon. Wea. Rev.,* **108,** 1607–1625.

Rothermel, J., C. Kessinger, and D. L. Davis, 1985: Dual-Doppler lidar measurement of winds in the JAWS experiment. *J. Atmos. Oceanic Technol.,* **2,** 138–147.

Tabary, P., and G. Scialom, 2001: MANDOP analysis over complex orography in the context of the MAP experiment. *J. Atmos. Oceanic Technol.,* **18,** 1293–1314.

Testud, J., and M. Chong, 1983: Three-dimensional wind field analysis from dual-Doppler radar data. Part I: Filtering, interpolating and differentiating the raw data. *J. Climate Appl. Meteor.,* **22,** 1204–1215.

Wakimoto, R., and R. Srivastava, 2003: *Radar and Atmospheric Science: A Collection of Essays in Honor of David Atlas. Meteor. Monogr.*, No. 30, Amer. Meteor. Soc., 270 pp.

Weber, B., and D. Wuertz, 1990: Comparison of rawinsonde and wind profiler radar measurements. *J. Atmos. Oceanic Technol.,* **7,** 157–174.

——, ——, R. Strauch, D. Merritt, and K. Moran, 1990: Preliminary evaluation of the first NOAA demonstration network wind profiler. *J. Atmos. Oceanic Technol.,* **7,** 909–918.

Weitkamp, C., 2005: *Lidar-Range-Resolved Optical Remote Sensing of the Atmosphere*. Springer Series in Optical Sciences, Vol. 102, Springer, 460 pp.

Xia, Q., C. H. Lin, and R. Calhoun, 2008: Retrieval of urban boundary layer structures from Doppler lidar data. Part I: Accuracy assessment. *J. Atmos. Sci.,* **65,** 3–20.